

RADIAL TRANSPORT OF LARGE-SCALE MAGNETIC FIELDS IN ACCRETION DISKS. II. RELAXATION TO STEADY STATES

TAKU TAKEUCHI¹ AND SATOSHI OKUZUMI

Department of Earth and Planetary Sciences, Tokyo Institute of Technology, Meguro-ku, Tokyo, 152-8551, Japan

Draft version January 20, 2020

ABSTRACT

We study the time evolution of a large-scale magnetic flux threading an accretion disk. Induction equation of the mean poloidal field is solved under the standard viscous disk model. Magnetic flux evolution is controlled by the two timescales: One is the timescale of the inward advection of the magnetic flux, τ_{adv} . This is induced by the dragging of the flux by the accreting gas. The other is the outward diffusion timescale of the magnetic flux τ_{dif} . We consider diffusion due to the Ohmic resistivity. These timescales can be significantly different from the disk viscous timescale τ_{disk} . The behaviors of the magnetic flux evolution is quite different depending on the magnitude relationship of the timescales τ_{adv} , τ_{dif} , and τ_{disk} . The most interesting phenomena occurs when $\tau_{adv} \ll \tau_{dif}, \tau_{disk}$. In such a case, the magnetic flux distribution approaches a quasi-steady profile much faster than the viscous evolution of the gas disk, and also the magnetic flux has been tightly bundled to the inner part of the disk. In the inner part, although the poloidal magnetic field becomes much stronger than the interstellar magnetic field, the field strength is limited to the maximum value that is analytically given by our previous work (Okuzumi et al. 2014, ApJ, 785, 127). We also find a condition for that the initial large magnetic flux, which is a fossil of the magnetic field dragging during the early phase of star formation, survives for a duration in which significant gas disk evolution proceeds.

Keywords: accretion, accretion disks — magnetic fields — MHD — planetary systems: protoplanetary disks

1. INTRODUCTION

Magnetic field is an important ingredient of the evolutionary process of accretion disks. A magnetic flux vertically threading a disk induces disk accretion via magneto-rotational instability (MRI; Balbus & Hawley 1998 for a review). It also accelerates disk winds via the magneto-centrifugal force (Blandford & Payne 1982) or the magnetic pressure (Shibata & Uchida 1985). The activity of these processes depends on the strength of the large scale magnetic field. For this reason, how the strength of large scale field is determined has been a key question in disk accretion processes.

A simple model on evolution of a large scale magnetic field threading an accretion disk was proposed by Lubow et al. (1994; henceforth LPP94). This model solves the evolution of the mean poloidal field, which is determined by the balance between inward dragging by the accreting gas and outward diffusion of the magnetic flux. Although this model neglects several important factors including the effect of the toroidal field, the analyses of this model have been providing us a useful guide in understanding the basic properties of the field transport in accretion disks (e.g., Shu et al. 2007; Cao 2011; Cao & Spruit 2013; Guilet & Ogilvie 2014).

Okuzumi et al. (2014; henceforth Paper I) have performed a comprehensive analysis on steady field profiles under the LPP94 model. They derived the maximum strength of the steady field, which is determined by the external field strength and the disk size (see Figure 7 of Paper I and see also Figure 9 of Guilet & Ogilvie 2014). This maximum field strength implies an upper limit on the accretion rate of disks due to MRI (Hawley

et al. 1995; Suzuki et al. 2010; Okuzumi & Hirose 2011; Gressel et al. 2012; Simon et al. 2013) and the mass loss rate due to magnetically driven wind (Blandford & Payne 1982; Bai & Stone 2013; Simon et al. 2013). The results of Paper I and Guilet & Ogilvie (2014) are thus providing significant predictions on the accretion and wind mass loss rates driven by the large scale magnetic field.

However, the analysis in Paper I was limited to steady state where inward field dragging balances with outward diffusion of the magnetic flux. Thus, the maximum field strength derived in Paper I is applicable only after the initial field has relaxed to a quasi-steady configuration. Before that, there remained the magnetic flux that had been dragged from the parent cloud core. This paper is devoted to analyzing how large-scale fields in disks evolve before the quasi-steady state has been reached.

Here, we briefly summarize the timescale argument in the LPP94 model. The relaxation timescale of mean poloidal fields is rh/η , where r the disk radius, h the disk thickness, and η is the magnetic diffusivity (Equation (21); see also Section 1 of Lovelace et. al. 2009). This is shorter than the disk evolution timescale, r^2/ν , where ν is the gas viscosity, provided that the magnetic Prandtl number $P_m = \nu/\eta$ is of order unity. Thus, quasi-steady fields in the disks are expected. LPP94 has shown, however, that the advection timescale of fields due to the drag by the accreting gas is also estimated as r^2/ν , meaning that inward dragging of the field is too weak to keep the magnetic flux against outward diffusion. The above discussion predicts that the initial field configuration quickly relaxes to a steady state. However, this argument also predicts that effective inward transport of the magnetic flux would not occur.

The above estimate of the timescales is based on the

¹ taku@geo.titech.ac.jp

assumption that the field advection takes place at the disk equatorial plane and the advection velocity of the field is similar to that of the gas. Ogilvie & Livio (2001) pointed out, however, that the gas drags the field mainly at a certain height where the electric conductivity is high. The advection velocity of the field would differ from the advection velocity of the gas at the midplane (Rothstein et al. 2008). If the field advection is much faster than the gas advection, it may be possible that the field relaxes to a quasi-steady configuration, in which a strong magnetic flux is still maintained in the disk. Guilet & Ogilvie (2014) has shown that such a situation is realized when the accretion velocity at the disk surface is much faster than that at the disk midplane. The vertical profile of the accretion velocity is yet unclear, and several papers have been devoted to studying the vertical structure of the disk (Lovelace et al. 2009; Bisnovatyi-Kogan & Lovelace 2013; Guilet & Ogilvie 2012, 2013).

This paper is the subsequent paper of Paper I, which has solved steady magnetic fields using the LPP94 model. The present paper studies the time evolution of the magnetic fields. We assume that the advection velocities of the gas and of the field are different. How much these velocities differ from each other depends on the vertical structure of the disk. Guilet & Ogilvie (2012, 2013) argued the possibility that the field advection velocity is more than 10 times greater than the gas advection. In this paper, we treat this factor, C_u , as a free parameter and solve the radial profile of the magnetic field. The vertically averaged magnetic Prandtl number, $P_{m,eff}$, is also treated as a free parameter.

The main purpose of this paper is to quantify the condition that the magnetic field relaxes to a steady state faster than the gas evolution, and that the field advection also occurs fast enough to keep a significant magnetic flux in the disk. We derive basic equations in Section 2. The main analytical result on the above condition is expressed on the $P_{m,eff}$ - C_u plane in Section 3, and is numerically verified in Section 4. If this condition is satisfied in realistic accretion disks, the maximum field strength in disks is limited by the prediction proposed in Paper I. The results are discussed in Section 5 and summarized in Section 6.

2. BASIC EQUATIONS

2.1. A Gas Disk

We consider an accretion disk which evolves via the “ α -viscosity”. The kinematic viscosity is written as $\nu = \alpha c_s h$, where c_s is the sound speed, h is the half thickness of the disk, and the parameter α is constant throughout the disk. The disk is assumed to be geometrically thin, with the ratio

$$\varepsilon = \frac{h}{r} \quad (1)$$

much smaller than unity. Using this prescription and the Keplerian rotation profile $\Omega(r) \propto r^{-3/2}$, the accretion velocity of the gas is written as (e.g., Frank et al. 1992)

$$\bar{u}_r = -\frac{3}{r^{1/2}\Sigma} \frac{\partial}{\partial r} \left(r^{1/2} \bar{\nu} \Sigma \right). \quad (2)$$

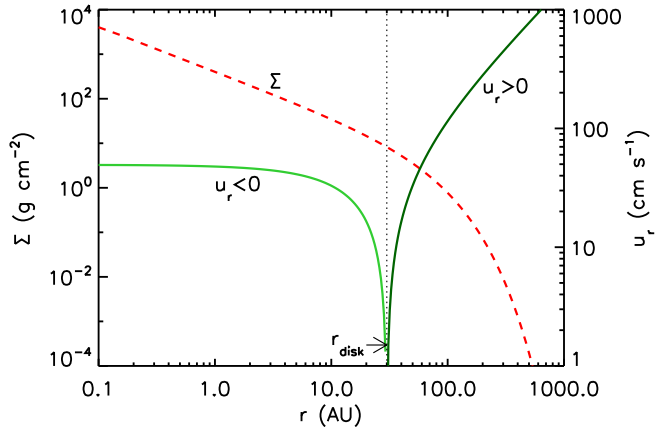


Figure 1. Structure of the gas disk. The red dashed line shows the surface density profile Σ . The green solid line shows the radial velocity u_r . The radial velocity is negative for $r < r_{disk}$ and positive for $r > r_{disk}$.

Here \bar{u}_r and $\bar{\nu}$ are mass-weighted vertical averages of the radial velocity and viscosity, respectively:

$$\bar{u}_r = \frac{\int_{-h}^h \rho u_r dz}{\int_{-h}^h \rho dz}, \quad \bar{\nu} = \frac{\int_{-h}^h \rho \nu dz}{\int_{-h}^h \rho dz}, \quad (3)$$

where ρ is the mass density of the gas. The evolution of the disk surface density is determined by

$$\frac{\partial \Sigma}{\partial t} - \frac{3}{r} \frac{\partial}{\partial r} \left[r^{1/2} \frac{\partial}{\partial r} \left(r^{1/2} \bar{\nu} \Sigma \right) \right] = 0. \quad (4)$$

Equation (4) has similarity solutions, when the viscosity profile obeys a power-law form, $\bar{\nu} = \bar{\nu}_0 (r/r_0)^\gamma$ (Lynden-Bell & Pringle 1974; Hartmann et al. 1998; Kitamura et al. 2002). The similarity solution is written as

$$\Sigma(r, t) = \Sigma_0 \left(\frac{r}{r_0} \right)^{-\gamma} T_g^{-\frac{5-2\gamma}{4-2\gamma}} \exp \left[-\frac{1}{2(2-\gamma)} \left(\frac{r}{r_{disk}} \right)^{2-\gamma} \right], \quad (5)$$

and

$$\bar{u}_r(r, t) = -\frac{3\bar{\nu}_0}{2r} \left(\frac{r}{r_0} \right)^\gamma \left[1 - \left(\frac{r}{r_{disk}} \right)^{2-\gamma} \right], \quad (6)$$

where

$$T_g = \frac{3(2-\gamma)\bar{\nu}_0}{2r_0^2} t + 1, \quad (7)$$

$$r_{disk}(t) = T_g^{1/(2-\gamma)} r_0. \quad (8)$$

Here T_g is the non-dimensional time scaled by the viscous time at r_0 , and r_{disk} is the disk size as such that the disk gas accretes ($\bar{u}_r < 0$) for $r < r_{disk}$ and it diffuses outward ($\bar{u}_r > 0$) for $r > r_{disk}$ (see Equation (6)). We define r_0 as the disk size at $t = 0$, i.e., $r_0 = r_{disk}(t = 0)$. This similarity solution is shown in Figure 1 for $r_{disk} = 30$ AU.

We consider a protoplanetary disk around a young star of $1M_\odot$ for numerical calculations. The temperature is assumed to be $T \propto r^{-q}$. The following parameters are

used for our fiducial model,

$$\varepsilon = 7.78 \times 10^{-2} \left(\frac{r}{r_0} \right)^{\frac{1-q}{2}}, \quad (9)$$

$$\bar{\nu} = 1.48 \times 10^{16} \left(\frac{r}{r_0} \right)^{\frac{3}{2}-q} \text{ cm}^2 \text{ s}^{-1}. \quad (10)$$

In the numerical calculations, we adopt $r_0 = 30\text{AU}$ and $q = 1/2$. The power-law index of the viscosity is $\gamma = 3/2 - q = 1$. The numerical values are calculated for $T = 278(r/1 \text{ AU})^{-1/2} \text{ K}$ and $\alpha = 10^{-2}$. The initial surface density is calculated from the mass accretion rate to the star, as $\Sigma_0 = \dot{M}/(3\pi\nu_0)$. For $\dot{M} = 3 \times 10^{-8} M_\odot \text{ yr}^{-1}$, $\Sigma_0 = 13.6 \text{ g cm}^{-2}$. (Note that Σ does not appear in the induction equation (13) and thus the above choice of Σ_0 does not affect the magnetic field evolution.)

2.2. Induction Equation

Magnetic field evolution is solved using the model proposed by LPP94. This model is the simplest model that describes the evolution of the poloidal magnetic flux threading an accretion disk. The toroidal field is neglected and the axisymmetric poloidal field is determined so as to connect to an external uniform field at infinity.

We consider evolution of the mean poloidal field threading a turbulent disk. The mean field inside the disk is calculated by Reynolds averaging of the turbulent field. Assuming that the mean poloidal field is axisymmetric, it is written by a flux function $\psi(r, z, t)$ as

$$B_r = -\frac{1}{r} \frac{\partial \psi}{\partial z}, \quad B_z = \frac{1}{r} \frac{\partial \psi}{\partial r}. \quad (11)$$

The induction equation for the mean poloidal field is, as shown by LPP94,

$$\frac{\partial \psi}{\partial t} = -u_r \frac{\partial \psi}{\partial r} - r\eta \frac{4\pi J_\phi}{c}, \quad (12)$$

where u_r is the mean radial velocity of the gas, η is the magnetic diffusivity, J_ϕ is the azimuthal current density, and c is the speed of light.

We average Equation (12) vertically in the following way. As pointed out by Ogilvie & Livio (2001), conductivity-weighted averaging is the proper way for averaging. Multiplying Equation (12) by the conductivity $\sigma_e = c^2/(4\pi\eta)$ and integrating over z , we obtain

$$\frac{\partial \psi}{\partial t} = -u_{r*} \frac{\partial \psi}{\partial r} - \frac{r\eta_*}{2h} \frac{4\pi K_\phi}{c}, \quad (13)$$

where $K_\phi = \int_{-h}^h J_\phi dz$ is the surface current density, and the subscript “*” means the conductivity-weighted averages, such that

$$u_{r*} = \frac{\int_{-h}^h \sigma_e u_r dz}{\int_{-h}^h \sigma_e dz} \quad (14)$$

$$\eta_* = \frac{\int_{-h}^h \sigma_e \eta dz}{\int_{-h}^h \sigma_e dz} = \frac{hc^2}{2\pi \int_{-h}^h \sigma_e dz}. \quad (15)$$

Here, the integration has been done from $-h$ to h , as in the mass-weighted vertical averaging (Equation (3)).

This is just a rough estimate. In reality, in the disk corona ($|z| > h_B$, where h_B is the height at which the magnetic pressure is same as the thermal pressure), the gas cannot drag the magnetic field and the current vanishes under our assumption of axisymmetric poloidal field. Thus, the integration in Equations (14) and (15) should be done for $|z| < h_B$, where the thermal pressure dominates the magnetic pressure, and it should be noted that h_B varies with the field strength. (See Guilet & Ogilvie (2012) for detailed discussion.) The surface current of the disk K_ϕ is related to ψ via the Biot-Savart equation,

$$\psi - \psi_\infty = \frac{r}{c} \int_{r_{in}}^{r_{out}} \int_0^{2\pi} \frac{K_\phi(r') \cos \phi' d\phi' r' dr'}{(r^2 + r'^2 - 2rr' \cos \phi')^{1/2}}, \quad (16)$$

where ψ_∞ is the flux of the external field. When the constant external field B_∞ is considered, we have

$$\psi_\infty = \frac{1}{2} B_\infty r^2. \quad (17)$$

Note that we have taken conductivity-weighted averaging for the induction equation, while mass-weighted averaging is used for the density evolution. In principle, u_{r*} is not necessary equal to \bar{u}_r . Therefore, we introduce a ratio of the average accretion velocities, C_u , as

$$u_{r*} = C_u \bar{u}_r. \quad (18)$$

The effective Prandtl number is defined by the ratio of the mass-weighted average of the gas viscosity to the conductivity-weighted average of the magnetic diffusivity,

$$P_{m,eff} = \frac{\bar{\nu}}{\eta_*}. \quad (19)$$

3. TIMESCALE ARGUMENT AND QUASI-STEADY STATES

From the equations for the gas and magnetic flux evolutions (Equations (4) and (13)), we define in Section 3.1 various evolution timescales, i.e., viscous timescale τ_{disk} , the diffusion timescale of the magnetic flux τ_{dif} , and the advection timescale of the magnetic flux τ_{adv} . In the following definition, we neglect numerical factors of order unity.

In section 3.2, we show that the behaviors of the magnetic flux evolution is quite different depending on the magnitude relationship of the timescales τ_{adv} , τ_{dif} , and τ_{disk} . The most interesting phenomena occurs when $\tau_{adv} \ll \tau_{dif}$, τ_{disk} . In such a case, the magnetic flux distribution approaches a quasi-steady profile much faster than the viscous evolution of the gas disk, and the magnetic flux has been tightly bundled to the inner part of the disk. In section 3.3, we derive the analytical flux profiles for the cases of $\tau_{adv} \ll \tau_{dif}$, τ_{disk} . These analytic expression was derived mainly in Paper I. In Appendix A, we expand the results of Paper I to include the effect of outward motion of the outer part of the viscous gas disk.

The argument in this section will be verified by the numerical integration of the basic equations in Section 4.

3.1. Various Evolution Timescales

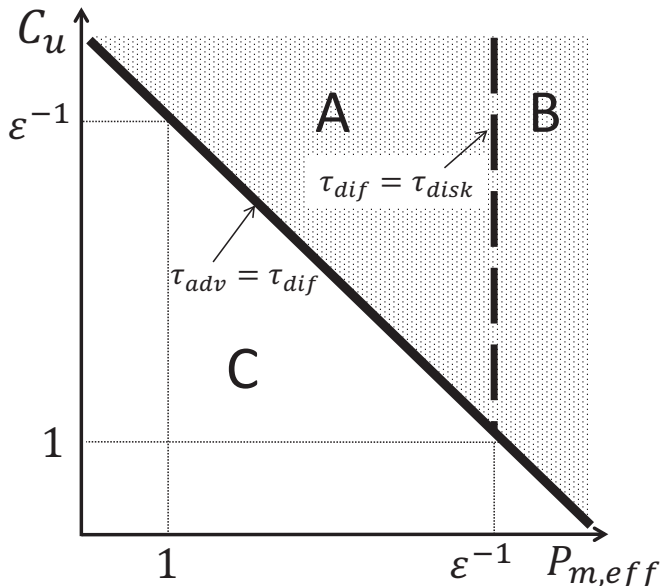


Figure 2. Various evolution regimes on the $P_{m,eff}$ - C_u plane. The solid and dashed lines indicate the boundaries where $\tau_{adv} = \tau_{dif}$ and $\tau_{dif} = \tau_{disk}$, respectively. In the shaded region ($\tau_{adv} < \tau_{dif}$), the effective field dragging by the gas takes place against the magnetic diffusion. This region is subdivided into regions A (where $\tau_{dif} < \tau_{disk}$) and B (where $\tau_{dif} > \tau_{disk}$). In region A, the magnetic field relaxes to a quasi-steady state rapidly within the disk evolution timescale. In region B, on the other hand, the initial profile of the magnetic field at the disk formation stage remains during gas disk evolution. In region C (where $\tau_{adv} > \tau_{dif}$) magnetic diffusion dominates over field advection, and therefore any magnetic flux except for externally imposed flux, ψ_∞ , is lost.

The viscous evolution of the gas disk is determined by Equation (4). Its timescale is given by

$$\tau_{disk} \equiv \frac{r_{disk}^2}{\bar{\nu}}. \quad (20)$$

The evolution timescale of the mean field is determined by the induction equation. The second term of the right hand side of Equation (13) causes diffusion of the magnetic field. The timescale of diffusion is estimated as $\tau_{dif} \sim (hc\psi)/(r\eta_*K_\phi)$. From the Biot-Savart equation (16), $K_\phi/c \sim \psi/r^2$ (see also Equations (29) of Paper I), and then the diffusion timescale is given by

$$\tau_{dif} \equiv \varepsilon P_{m,eff} \tau_{disk}. \quad (21)$$

This means that the diffusion timescale of the magnetic field is shorter than that of the gas evolution timescale, as long as $P_{m,eff} \leq \varepsilon^{-1}$. If $P_{m,eff} \sim 1$, as usually expected, the magnetic field relaxes quickly to a quasi-steady state within the disk evolution timescale.

The first term of the right hand side of Equation (13) represents the advection of the magnetic field. The timescale of advection is estimated as $\tau_{adv} \sim r/u_{r*}$. From Equation (18) and $\bar{u}_r \sim \bar{\nu}/r$, the advection timescale is given by

$$\tau_{adv} \equiv C_u^{-1} \tau_{disk}. \quad (22)$$

Thus, if $C_u > 1$, the advection timescale of the magnetic field is shorter than the gas evolution timescale.

3.2. Comparison of Timescales

The condition for effective field advection to the inner part of the disk is $\tau_{adv} < \tau_{dif}$. This condition reduces to

$$C_u P_{m,eff} > \varepsilon^{-1}, \quad (23)$$

and is shown by the shaded region on the $P_{m,eff}$ - C_u plane in Figure 2.

Effective field advection ($\tau_{adv} \ll \tau_{dif}$) takes place either if $C_u > \varepsilon^{-1}$ or if $P_{m,eff} > \varepsilon^{-1}$. First, we consider a case in which $C_u > \varepsilon^{-1}$ and $P_{m,eff} \sim 1$. In this case, the magnetic field relaxes to a quasi-steady state more quickly compared to the disk evolution ($\tau_{dif} \ll \tau_{disk}$). Thus, the profile of the magnetic field at any evolutionary stages should be given by the steady profile discussed in Section 3.5 below, except at early stages. This regime is shown as the “region A” in Figure 2.

If the effective field advection is supported by large values of $P_{m,eff} > \varepsilon^{-1}$ rather than by large C_u , then the magnetic diffusion timescale $\tau_{dif} = P_{m,eff} \varepsilon \tau_{disk}$ is also longer than the disk evolution timescale τ_{disk} . In such cases, the magnetic field remembers its initial profile that was set at the formation stage of the disk. This regime is shown as the “region B” in Figure 2.

Finally, in the “region C” in Figure 2, the condition for significant field advection given by Equation (23) is not satisfied. In such cases, disk accretion cannot drag the magnetic field effectively. Even if a strong concentration of the magnetic flux at the inner disk was created during the disk formation stage, the magnetic flux diffuses outward with a timescale τ_{dif} , which is expected to be shorter than the disk evolution timescale τ_{disk} (as long as $P_{m,eff} < \varepsilon^{-1}$).

We stress that in the region A, i.e., if $\tau_{adv} \ll \tau_{dif} \ll \tau_{disk}$, a large-scale magnetic field in an accretion disk has been transferred to the inner part of the disk and relaxes into a quasi-steady state. This interesting regime will be discussed in detail in the next subsection.

3.3. Quasi-Steady Profile of the Magnetic Field for Strong Dragging

In this subsection, we focus on the region A in Figure 2, in which most of the magnetic flux that initially threaded the disk have been transported to the inner part of the disk. We derive the quasi-steady profiles of the magnetic field under given density and velocity profiles of the gas disk. Setting $\partial/\partial t = 0$, Equation (13) becomes

$$B_z - \frac{D}{2} \frac{4\pi K_\phi}{c} = 0, \quad (24)$$

where

$$D = -\frac{\eta_*}{u_{r*} h} = -\frac{1}{P_{m,eff} C_u \varepsilon} \frac{\bar{\nu}}{\bar{u}_r r}, \quad (25)$$

denotes the effective diffusivity compared to the advection. For disks with smooth density and velocity profiles, $\bar{\nu}/(\bar{u}_r r) \sim 1$. Thus the magnitude of D is roughly estimated as

$$|D| \sim (P_{m,eff} C_u \varepsilon)^{-1} = \frac{\tau_{adv}}{\tau_{dif}}. \quad (26)$$

For significant field advection, $|D| \ll 1$ is required.

3.4. A Toy Model for a Gas Disk

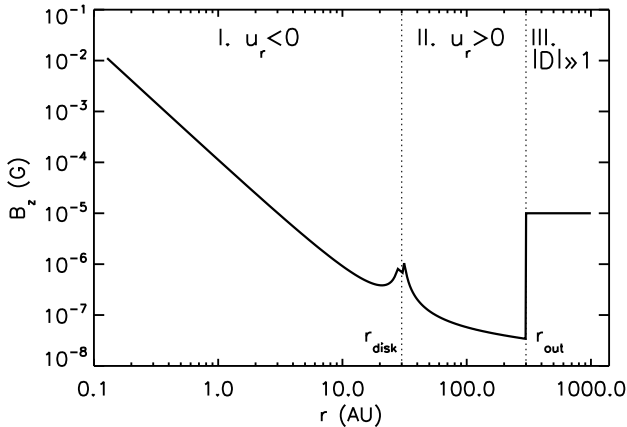


Figure 3. Quasi-steady profile of the magnetic field, B_{stdy} , calculated by Equation (28) for the gas disk shown in Figure 1. We set $P_{m,eff}C_u = 100$ for $r < r_{out}$. The spurious feature at r_{disk} is an artifact of the approximate expression (see text). The disk is divided at r_{disk} and r_{out} .

As shown in Figure 1, the inner part of the disk ($r < r_{disk}$) accretes to the star and the outer part diffuses outward. The magnetic field is dragged to the same direction of this gas motion. In the outer part, the gas density declines exponentially with the radius, and at the outer edge it becomes so tenuous that the gas pressure becomes lower than the magnetic pressure or that the ambipolar diffusion suppresses the MRI (Walsh et al. 2012; Dzyurkevich et al. 2013). Thus, at the outermost part, the gas cannot drag the magnetic field effectively. This region is modeled by a large effective diffusivity D .

The disk is divided into three parts: I. the inner accreting region, II. the outer region where the gas moves outward, and III. the outermost part where the gas cannot drag the magnetic field. These parts are characterized as,

$$\begin{cases} \text{I. } \bar{u}_r < 0 & \text{for } r < r_{disk} \\ \text{II. } \bar{u}_r > 0 & \text{for } r_{disk} < r < r_{out} \\ \text{III. } |D| \gg 1 & \text{for } r > r_{out} \end{cases}, \quad (27)$$

as shown in Figure 3.

3.5. Approximate Steady Profile of the Magnetic Field for Strong Dragging

Steady solutions of the magnetic field have been derived in Paper I, assuming that advection of the field is inward everywhere. As described in Section 3.4, we consider disks with both outward and inward advectons. We derive in Appendix A an approximate formula for the field strength in such disks. Assuming that the field dragging is strong in the main body of the disk ($|D| \ll 1$ for $r < r_{out}$), the vertical field strength is approximately written as

$$B_{stdy} = \begin{cases} 2\gamma_c |D| \left(\frac{r_{disk}}{r_{out}} \right) \left(\frac{r}{r_{disk}} \right)^{-2} B_\infty & \text{for } r < r_{disk} \\ \frac{2|D|}{\pi} \left(\frac{r}{r_{out}} \right) B_\infty & \text{for } r_{disk} < r < r_{out} \\ B_\infty & \text{for } r > r_{out} \end{cases}, \quad (28)$$

where the numerical factor $\gamma_c = 0.43$.

An example of the vertical field strength is shown in Figure 3. We set $P_{m,eff}C_u = 100$ for $r < r_{out}$

($\tau_{dif}/\tau_{adv} = 100\varepsilon$), making $|D| \approx 0.2 - 0.3$ for $r < r_{disk}$ and $|D| \sim 0.1 - 0.01$ for $r_{disk} < r < r_{out}$. For $r > r_{out}$, we assume $|D| \gg 1$, and thus $B_{stdy} = B_\infty$. The profile reflects the r dependence of $|D|$. The magnetic field profile shown in Figure 3 decreases with r even in region II. It seems to be at odds with Equation (28) and Figure 11. This behavior of B_{stdy} comes from the fact that $|D|$ is a decreasing function of r . In the region II (and for $r \gg r_{disk}$), $\bar{v} \propto r$, $\bar{u}_r \propto r$, $\varepsilon \propto r^{1/4}$, and then $|D| \propto r^{-5/4}$. Further, $|D|$ becomes greater than unity when approaching r_{disk} , because $\bar{u}_r(r_{disk}) = 0$. Equation (28) is appropriate only for $|D| \ll 1$. In Figure 3, $|D|$ in Equation (28) was replaced by $\min(|D|, 1)$, which causes a spurious feature of the field profile around r_{disk} . This feature is actually not reproduced by the numerical calculation shown in Section 4. We see that the magnetic field profiles in Figure 5-9 are smooth around r_{disk} , and thus the spurious feature in the approximate expression should be considered as artificial.

Note that at the inner disk ($r < r_{disk}$) where the magnetic flux moves inward, the field profile approaches $B_{stdy} \propto r^{-2}$ for $|D| \rightarrow 0^2$ as shown in Figure 8 of Paper I and in Figure 2 of Guilet & Ogilvie (2014). This means that for $|D| \ll 1$ the magnetic flux, $\psi = \int r B_z dr \propto \log r$, concentrates at the innermost part of the disk. For weaker field dragging ($|D| \sim 1$; see section 4.3 and Figure 9 below), though the magnetic field B_{stdy} looks to be still advected to the inner part, concentration of the magnetic flux is more milder (see also Paper I; Guilet & Ogilvie 2014), and consequently the magnetic flux $\psi(r)$ extends in the whole disk. In this paper we consider that tight bundling of the magnetic flux occurs when $|D| \ll 1$.

4. TIME EVOLUTION OF THE MAGNETIC FIELD

In this section, we discuss the time evolution of the disk gas and the magnetic field. Induction Equation (13) is numerically solved under the evolution of the gas disk described by the similarity solution (6). Note that only the velocity profile $\bar{u}_r(r)$ is needed.

The numerical method solving Equation(13) is similar to that by LPP94. The computational domain is $[0.1\text{AU}, 10^3\text{AU}]$, and 400 grid points are used with spacing in proportion to $r^{1/2}$. The disk region III where $|D| \gg 1$ is realized by setting $C_u = 0.1$ (Case A; Section 4.1) or $P_{m,eff} = 0.1$ (Case B and C; Section 4.2 and 4.3) for $r > r_{out}$. For numerical stability, we further set $u_{r*} = 0$ for $r > 800\text{AU}$.

The initial profile of the gas disk is shown in Figure 1. We consider two types of initial profiles with different vertical field strength. The first one is the uniform external field B_∞ . This represents an extreme case in which magnetic flux concentration has not occurred in the disk formation phase. The second one represents a strong initial concentration of the magnetic flux. In Paper I, we have discussed that the maximum field strength in a steady state is expected to be

$$B_{\max} = \begin{cases} \left(\frac{r}{r_{out}} \right)^{-2} B_\infty & \text{for } r < r_{out} \\ B_\infty & \text{for } r > r_{out} \end{cases} \quad (29)$$

² We neglect in this paragraph r dependence of D . In our model, $D \propto \varepsilon^{-1} \propto r^{-0.25}$, but this weak dependence does not change the conclusion of this paragraph that $|D| \ll 1$ is required for the magnetic flux to be tightly bundled.

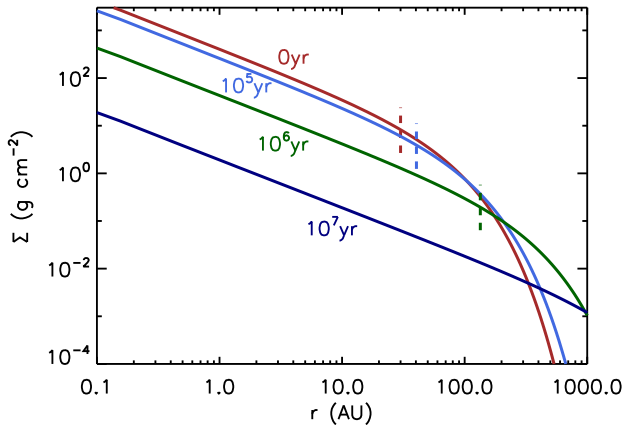


Figure 4. Evolution of the gas density profile. The gas evolves self-similarly. The locations where the gas velocity switches from inward to outward are shown by the dashed vertical lines plotted on the density profiles.

We set $B_z(t=0) = B_{\max}$ for the second extreme case.

The evolution of the gas disk is shown in Figure 4. The evolution timescale at the initial state is $\tau_{disk} \sim r_0^2/\bar{v}_0 \sim 4 \times 10^5 \text{yr}$, where disk radius $r_0 = 30 \text{AU}$ at $t = 0$. As the disk evolves, its evolution timescale increases, because the disk radius expands. In Figure 4 the locations of r_{disk} are shown by the dashed lines marked on the density profiles. It is apparent that r_{disk} moves outward with time.

4.1. Case A: $\tau_{dif} = \varepsilon\tau_{disk}$ and $\tau_{adv} = 10^{-2}\tau_{disk}$ ($C_u = 100$ and $P_{m,eff} = 1$)

First, we consider the case with $C_u = 100$ and $P_{m,eff} = 1$. This corresponds to region A in Figure 2. Figure 5 shows the evolution of the initially uniform field $B_z = B_\infty$ at $t = 0$. The magnetic flux is advected inward for $r < r_{disk}$ and outward for $r > r_{disk}$. Because the advection timescale is shorter for smaller r , the field profile approaches the quasi-steady state from inside (Figure 5b), and the part inside r_{disk} becomes nearly quasi-steady state at $t = \tau_{adv} = C_u^{-1}\tau_{disk} \approx 4 \times 10^3 \text{yr}$ (Figure 5c). Then, the magnetic flux outside r_{disk} is expelled due to outward gas migration. The outward advection velocity of the field is $u_{r*} \propto r$ (Equation (6) with $\gamma = 1$), and the advection timescale outside r_{disk} is nearly independent of r , i.e., $r/u_{r*} \approx r_{disk}/u_{r*}(r_{disk}) = \tau_{adv}$. Thus, the field profile outside r_{disk} quickly evolves with the timescale at r_{disk} even for larger r . It takes several times more than τ_{adv} for relaxation to the quasi-steady state in the whole disk, because the initial field profile is quite different from the quasi-steady field by orders of magnitude. The whole field profile becomes almost the quasi-steady state in $t = 10^4 \text{yr}$ (Figure 5d), which is much earlier than $\tau_{disk}(t=0) \sim 4 \times 10^5 \text{yr}$, where we used $\varepsilon = 7.7 \times 10^{-2}$ at $r_0 = 30 \text{AU}$. After field relaxation, the magnetic field evolves as such that its profile keeps the quasi-steady profile B_{stdy} , as seen in Figure 5e. Finally, in Figure 5f at 10^7yr , the disk radius r_{disk} has expanded beyond r_{out} , outside which the gas cannot drag the magnetic field. The magnetic field shown in Figure 5f is the final profile without further evolution, provided that r_{out} is fixed. The evolutionary sequence shown in Figure 5 is

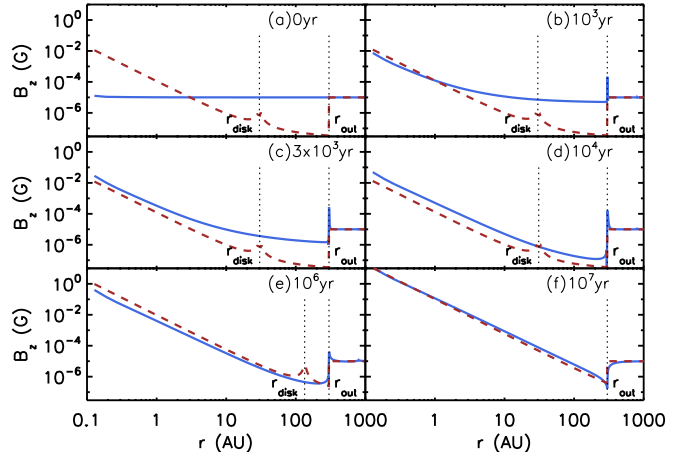


Figure 5. Evolution of the magnetic field, B_z , for the case where $C_u = 100$, $P_{m,eff} = 1$ ($\tau_{dif} = \varepsilon\tau_{disk}$, $\tau_{adv} = 10^{-2}\tau_{disk}$), and the initial profile of $B_z = B_\infty$. The blue solid line shows the result of numerical integration. The brown dashed line shows the approximate steady field calculated by Equation (28) for the gas disk profile at each time. The vertical dotted lines show the radii r_{disk} and r_{out} .

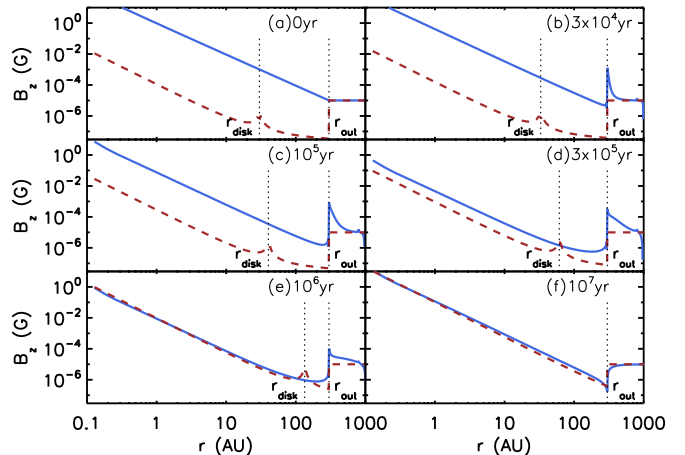


Figure 6. Evolution of the magnetic field, B_z , for the case where $C_u = 100$, $P_{m,eff} = 1$ ($\tau_{dif} = \varepsilon\tau_{disk}$, $\tau_{adv} = 10^{-2}\tau_{disk}$), and the initial profile of $B_z = B_{\max}$. The blue solid line shows the result of numerical integration and the brown dashed line shows the approximate steady solution.

controlled mainly by advection. This is consistent with the analytical picture described in Figure 4 of Guilet & Ogilvie (2014).

Figure 6 shows the evolution of the magnetic field which is concentrated to the center at $t = 0$. The initial profile $B_z = B_{\max} \propto r^{-2}$ is given by Equation (29). The magnetic flux is confined to the innermost part of the disk ($\psi(r) \propto \log r$). In this case, the evolution is controlled mainly by outward diffusion of the flux to r_{disk} . The flux outside r_{disk} is quickly advected to r_{out} by the outward migrating gas with timescale $\tau_{adv} (< \tau_{disk})$, as discussed in the last paragraph. Actually, in the numerical solution, evolution due to magnetic diffusion appears at $t = 3 \times 10^4 \approx \tau_{dif}$ (Figure 6b), and the magnetic field profiles has nearly relaxed to the quasi-steady state by $t = 3 \times 10^5 \approx 10\tau_{dif}(t=0)$ (Figure 6d). It takes about $10\tau_{dif}(t=0)$ for relaxation, because the initial

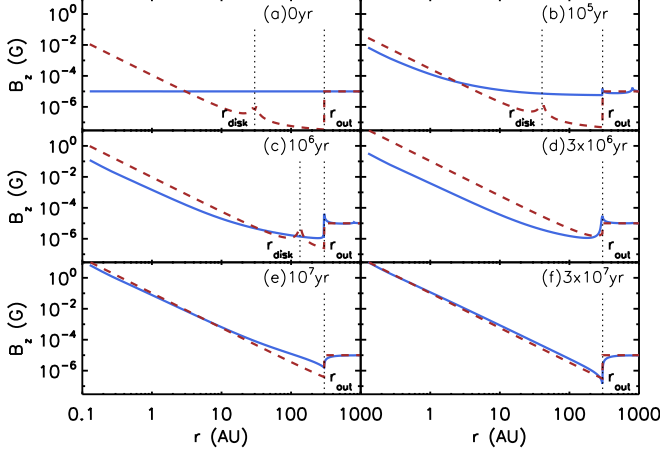


Figure 7. Evolution of the magnetic field, B_z , for the case where $C_u = 1$, $P_{m,eff} = 100$ ($\tau_{dif} = 100\varepsilon\tau_{disk}$, $\tau_{adv} = \tau_{disk}$), and the initial profile of $B_z = \tilde{B}_\infty$. The blue solid line shows the result of numerical integration and the brown dashed line shows the approximate steady solution.

field is about 10^3 times stronger than the quasi-steady field (compare the solid line in Figure 6a and the dashed line in Figure 6d), and also because τ_{dif} increases as r_{disk} moves to 60 AU by 3×10^5 yr. Further evolution is similar to the case of the initially uniform field in Figure 5, i.e., the magnetic field is in the quasi-steady state (Figures 6e and f).

The above numerical experiments with two extreme initial conditions show that, if the effective magnetic Prandtl number $P_{m,eff}$ is of order unity, the magnetic field quickly relaxes to the quasi-steady profile B_{stdy} . The relaxation timescale is several times the characteristic timescale either of advection, $\tau_{adv} = C_u^{-1}\tau_{disk}$, or of diffusion, $\tau_{dif} = \varepsilon P_{m,eff}\tau_{disk}$, depending on the initial field profile. It is shorter than the gas evolution timescale unless the initial magnetic flux in the disk is too strong. Thus, except for a beginning stage of the gas evolution, the steady solution derived in Paper I gives plausible estimates for the magnetic field strength of actual disks.

4.2. Case B: $\tau_{dif} = 100\varepsilon\tau_{disk}$ and $\tau_{adv} = \tau_{disk}$ ($C_u = 1$ and $P_{m,eff} = 100$)

In this section, we consider the case in which $C_u = 1$ and $P_{m,eff} = 100$, which corresponds to region B in Figure 2. Inward field advection is maintained by large effective Prandtl number $P_{m,eff}$, not by high advection speed of the magnetic field ($C_u = 1$). Under the above parameters, the diffusion timescale of the magnetic field is $\tau_{dif} \sim P_{m,eff}\varepsilon\tau_{disk} \sim 3 \times 10^6$ yr, which is much slower than the disk evolution timescale τ_{disk} . Figures 7 and 8 show that the magnetic field remembers the initial profile more than 10^7 yr. The field relaxes to the steady state after 3×10^7 yr, but at that time the disk has already experienced considerable evolution. These calculations have shown that the steady solution derived in Paper I would not be appropriate in Case B.

The numerical calculations sometimes result in negative values of B_z around r_{out} , that are shown by the light-blue lines in Figures 8b–e. This negative B_z originates from our simplified formalism of the field evolution and the initial condition adopted here. At the initial

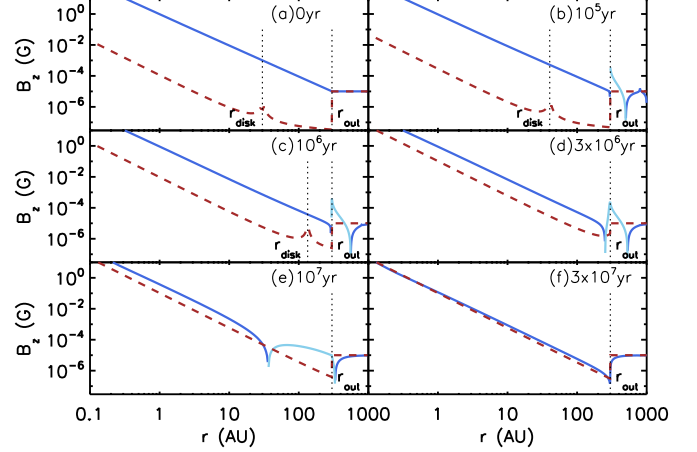


Figure 8. Evolution of the magnetic field, B_z , for the case where $C_u = 1$, $P_{m,eff} = 100$ ($\tau_{dif} = 100\varepsilon\tau_{disk}$, $\tau_{adv} = \tau_{disk}$), and the initial profile of $B_z = B_{max}$. The blue solid line shows the result of numerical integration and the brown dashed line shows the approximate steady solution. The part shown by the light blue line has the negative values of B_z .

state shown in Figure 8a, the magnetic field is much stronger than that expected as the quasi-steady state (the dashed line). The magnetic flux inside r_{out} is also much stronger than the analytical upper limit $2\pi r_{out}^2 B_\infty$ derived by Okuzumi et al. (2014). Such a strong concentration of the magnetic flux at the initial state is maintained not only by the toroidal current inside r_{out} but also by the current outside r_{out} . Because we assume $P_{m,eff} = 0.1$ outside r_{out} , the current there quickly dissipates, while the current inside r_{out} remains for much longer time. The remaining current especially at r_{out} generates negative B_z . (Negative B_z appears even when we set $P_{m,eff} = 1$ outside r_{out} .) Note that appearance of negative B_z means formation of closed field lines connecting different radii in the differentially rotating disk. They should give rise to toroidal fields that are ignored in our model, suggesting that field evolution in Figure 8 is not self-consistent. The negative B_z disappears by 3×10^7 yr and the quasi-steady state is finally realized (Figure 8f). Because this relaxation timescale is similar to that with the initially uniform field in Figure 7, we expect our qualitative conclusion on the relaxation timescale is correct, but it should be examined by a more sophisticated model.

4.3. Case C: $\tau_{dif} = 10\varepsilon\tau_{disk}$ and $\tau_{adv} = \tau_{disk}$ ($C_u = 1$ and $P_{m,eff} = 10$)

If $C_u P_{m,eff} < \varepsilon^{-1}$ ($|D| \gtrsim 1$), the magnetic flux diffuses outward more quickly compared to the inward field advection. Figure 9 shows the magnetic field evolution with $C_u = 1$ and $P_{m,eff} = 10$. Initial field profile $B_z(t=0) = B_{max}$ shows concentration of the flux toward $r = 0$. This flux that initially concentrated to the center diffuses outward, and at 10^7 yr the profile reaches a steady state, which shows only weak concentration of the flux at the center. The brown line in Figure 9 shows the quasi-steady profile given by Equation (28), which assumes $|D| \ll 1$. Here, actual $|D| \sim (P_{m,eff} C_u \varepsilon)^{-1} \sim 1$, and the resultant magnetic field is much weaker than the field strength expected for cases A and B with strong

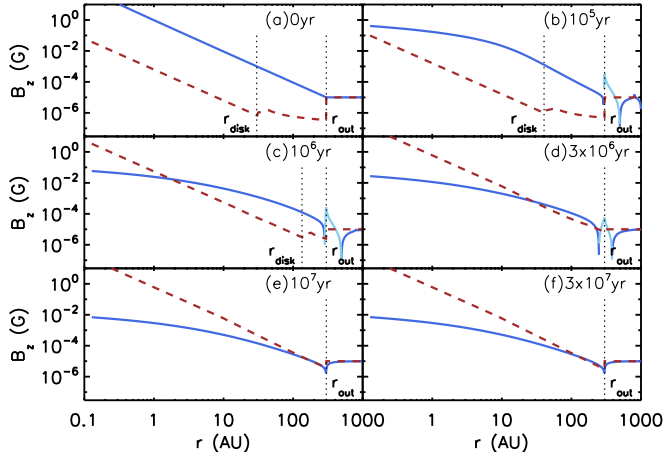


Figure 9. Evolution of the magnetic field, B_z , for the case where $C_u = 1$, $P_{m,eff} = 10$ ($\tau_{dif} = 10\varepsilon\tau_{disk}$, $\tau_{adv} = \tau_{disk}$), and the initial profile of $B_z = B_{max}$. The blue solid line shows the result of numerical integration and the brown dashed line shows the approximate steady solution. The part shown by the light blue line has the negative values of B_z .

inward dragging. This result confirms the conclusion of LPP94 that strong field dragging (or flux concentration to the inner part) requires $|D| \ll 1$.

5. DISCUSSIONS

5.1. Dependence of r_{out}

We used a fixed value $r_{out} = 300\text{AU}$ for simplicity in the numerical calculations in Section 4. The steady profile described in Section 3.5 depends on r_{out} (Equation(28)). Thus, r_{out} is an important parameter for determining the magnetic field strength in (quasi-)steady states. In real disks, r_{out} should be determined as the radius outside which the gas can no longer drag the field effectively. Determining r_{out} requires further investigations on the tenuous outermost part of disks.

The evolutionary sequences described in Section 4 do not depend on the value of r_{out} . Time evolutions of the magnetic field are classified into three regimes A-C in Figure 2, based on $P_{m,eff}$ and C_u . Each regime is characterized via comparison of the several evolution timescales, which are evaluated at r_{disk} , not at r_{out} . Thus, r_{out} does not affect the classification in Figure 2. To see this, we have performed additional calculations with a different assumption on r_{out} . In those additional calculations, we assume that the boundary between the regions II and III in Figure 3 is determined by the density, i.e., r_{out} is calculated from the condition $\Sigma(r_{out}) = \Sigma_c$, where Σ_c is the threshold value. As Σ evolves with time, r_{out} varies. We performed calculations for $\Sigma_c = 10^{-2}$, 0.1, and 1, and confirmed that the classification of the evolutionary sequences does not depend on r_{out} .

5.2. Vertical Structure of the Disk

In Section 3, the advection and diffusion timescales were discussed. Estimate of the timescales is based on induction equation (13), which is vertically averaged with conductivity weighting. (We call $1/\eta$ as conductivity.) The differences between the conductivity-weighted and mass-weighted averages are expressed by the parameters $P_{m,eff}$ and C_u given by Equations (18) and (19). In this

paper, we treat $P_{m,eff}$ and C_u as free parameters and see how the magnetic field evolution is controlled by these parameters. In reality, averaging requires knowledge of the vertical structure of the disk, such as $\eta(z)$, $\nu(z)$, and $u_r(z)$.

In protoplanetary disks, the ionization degree decreases with the depth from the disk surface (Sano et al. 2000), and thus the Ohmic resistivity increases with the depth. In disks with MRI turbulence, turbulent resistivity would be added. The MRI is active around a certain height which is above the dead zone around the midplane (if present) and which is below the disk corona. At the disk corona, ambipolar diffusion is responsible for the magnetic diffusivity. To determine the height dependence of the magnetic diffusivity, contribution of Ohmic, turbulent, and ambipolar diffusivities should be calculated. There have been calculations of Ohmic and ambipolar diffusivities in laminar stratified disks (Walsh et al. 2012; Dzyurkevich et al. 2013), and also numerical simulations of measuring the turbulent diffusivity in a local shearing box (Guan & Gammie 2009; Lesur & Longaretti 2009; Fromang & Stone 2009). We need to combine these results and measure the total diffusivity in the turbulent stratified disk by numerical simulations.

Vertical profile of the gas velocity $u_r(z)$ is also important, because the conductivity-weighted average u_{r*} is dominated by $u_r(z)$ at specific regions where $\eta(z)$ has a minimum value which possibly occurs at the surface of the disk. If $|u_r|$ is an increasing function of $|z|$, $C_u = u_{r*}/\bar{u}_r$ could be much larger than unity and also would be larger for higher β_z (see the lower left panel of Figure 8 in Guilet & Ogilvie 2012). If C_u is expressed by a function of β_z and $P_{m,eff}$, then Figure 2 can be converted on the $P_{m,eff}$ - β_z plane. As an example, using the results shown in Figure 12 of Guilet & Ogilvie (2012), the boundary between the hatched region and region C ($\tau_{adv} = \tau_{dif}$) corresponds to $\beta_z = 10^3$ for $P_{m,eff} = 1$ and $\beta_z = 1$ for $P_{m,eff} = \varepsilon^{-1}$. Note that these values could be quite different for other disk models, depending on the vertical structure of the disk.

6. SUMMARY

We have studied the time evolution of a large-scale magnetic flux threading an accretion disk. Induction equation of the mean poloidal field is solved for a viscously evolving disks.

We use mass-weighted averaging for the equation of surface density evolution, while conductivity-weighted averaging is used for the induction equation, according to suggestion by Ogilvie & Livio (2001). In a thin disk approximation, fluid equations and induction equation are averaged in the vertical direction. While mass-weighted averaging method is useful for gas dynamics, conductivity-weighted averaging method is more appropriate for magnetic flux evolution. There may be differences between these two methods. The ratios between the mass-weighted and conductivity weighted averages (C_u and $P_{m,eff}$ defined in Equations (18) and (19)) are the important parameters determining the evolution timescales of the gas and magnetic flux.

The ratio of the magnetic field evolution timescale to the disk evolution timescale is controlled by the parameter C_u and $P_{m,eff}$. The diffusion timescale of the magnetic flux τ_{dif} is $\varepsilon P_{m,eff}$ times the disk evo-

lution timescale, τ_{disk} , where $\varepsilon \ll 1$ is the geometric aspect ratio of the disk ($\tau_{dif} = \varepsilon P_{m,eff} \tau_{disk}$). The advection timescale of the magnetic flux is written as $\tau_{adv} = C_u^{-1} \tau_{disk}$. The evolution of the magnetic flux can be categorized by these timescales (or the parameters $P_{m,eff}$ and C_u^{-1}).

Using these timescales we categorize evolutionary types of magnetic fields. If $\tau_{dif} \ll \tau_{disk}$ (or $P_{m,eff} \lesssim \varepsilon^{-1}$), the magnetic flux quickly relaxes to a quasi-steady profile. Thus, the field profile in each evolutionary phase of the gas disk is given by the steady profiles discussed in Paper I. Further, if $\tau_{adv} \ll \tau_{disk}$ (or $C_u \gg 1$) is satisfied at the same time, the magnetic flux profiles would have relaxed to a quasi-steady state in which the flux would be tightly bundled at the inner part of the disk. This regime of the magnetic flux evolution is shown in Figure 2 as the region A. On the other hand, even if $\tau_{adv} \ll \tau_{disk}$, in the case of $\tau_{dif} \gtrsim \tau_{disk}$ (or $P_{m,eff} \gtrsim \varepsilon^{-1}$), the initial profile of the magnetic flux remains longer than the disk evolution timescale. In this case, the initial disk formation phase is important for determining later magnetic flux evolution. This evolutionary regime is the region B in Figure 2. Finally, if $\tau_{dif} \ll \tau_{adv}$ (or $C_u P_{m,eff} < \varepsilon^{-1}$), the accreting gas cannot drag the magnetic flux significantly, and only weak concentration of the magnetic flux in the disk is expected. This regime is shown as the region C in Figure 2.

This paper treats $P_{m,eff}$ and C_u as free parameters, and we do not specify the timescales τ_{dif} and τ_{adv} . In reality, these should be physically determined via the vertical structure of the disk and field lines. The key issues are the height where the magnetic field dragging occurs most effectively (Ogilvie & Livio 2001; Rothstein et al. 2008) and the angular momentum extract by the disk wind

(Bisnovatyi-Kogan & Lovelace (2012); Guilet & Ogilvie (2012)). The efficiency of field dragging should be determined by future investigations on vertical dependences of $u_r(z)$, $\nu(z)$, and $\eta(z)$ and structure of field lines. How much the disk wind would extract the angular momentum from the disk also should be quantified.

Finally, we should note that this paper is based on the LPP94 model in which any effect due to toroidal fields is ignored. Toroidal fields transfer angular momentum along \mathbf{B} , and possibly launch disk wind, which extract the angular momentum from the disk. Global evolution of magnetic fields for wind driven accreting disks is an important topic. Further, presence of the disk wind may cause a toroidal current above the Alfvén surface. Ogilvie (1997) discussed that the effect of the toroidal current outside the Alfvén surface effectively works as modifying the external field \mathbf{B}_∞ , which is the boundary condition in the LPP94 model at infinity. With this modification, the field configuration and the flux transport inside the Alfvén surface can be treated by the LPP94 model. However, how much \mathbf{B}_∞ is modified by the wind has not been clear and needs to be quantified in future works.

We thank Takayuki Muto for useful discussions and Junko Kominami for careful reading of the manuscript. We appreciate the anonymous referee for his/her thorough review that helped us to improve the quality of the paper and to find errors in the original version of the manuscript. This work was supported by Grants-in-Aid for Scientific Research, Nos. 20540232, 23103005, 25887023, 26103704, and 26400224 from MEXT of Japan.

APPENDIX

STEADY PROFILE OF THE MAGNETIC FIELD UNDER OUTWARD ADVECTION

We have derived in Paper I the approximate expressions of the steady magnetic profiles in accretion disks, assuming that advection of the magnetic field is inward everywhere in the disk. In reality, the advection is outward in the outer part of disks. In this Appendix, we derive the approximate expressions of the magnetic field profiles in disks with outward motions.

The vertically averaged induction equation is

$$B_z = \frac{D}{2} \frac{4\pi K_\phi}{c}, \quad (\text{A1})$$

where D is negative for outward advection ($u_{r*} > 0$). We first consider a piecewise profile of D as

$$D = \begin{cases} D_{II} & \text{for } r_{in} < r < r_{out} \\ \infty & \text{otherwise} \end{cases}, \quad (\text{A2})$$

where D_{II} is negative and $|D_{II}| \ll 1$.

The numerical solution of Equation (A1) is shown in Figure 10. We set $r_{in} = 10^{-2}$, $r_{out} = 1$, and $D_{II} = -0.1$. From Figure 10, it is apparent that $B_z \ll B_\infty$ for $r < r_{out}$. Thus, most of the imposed external flux, $\psi_\infty = B_\infty r^2/2$, has been expelled from the disk. The resultant magnetic flux ψ is almost zero for $r < r_{out}$ compared to ψ_∞ . For $r_{in} < r < r_{out}$, the vertical field strength is proportional to r , in contrast to the inward advection case (positive D) where $B_z \propto r^{-2}$.

The profile of the magnetic field is approximately expressed by

$$B_z = \begin{cases} 2\gamma_c \left(\frac{r_{in}}{r_{out}}\right) B_\infty & \text{for } r < r_{in} \\ \frac{2|D|}{\pi} \left(\frac{r}{r_{out}}\right) B_\infty & \text{for } r_{in} < r < r_{out} \\ B_\infty & \text{for } r > r_{out} \end{cases}, \quad (\text{A3})$$

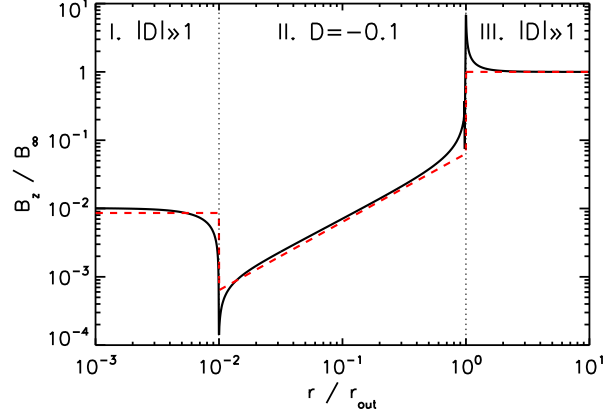


Figure 10. Steady profile of the magnetic field for piecewise constant D . The solid line is numerically calculated, and the dashed line shows the approximate expression given by Equation (A3).

which is shown by the red dashed line in Figure 10. In Equation (A3), $\gamma_c = 0.43$ is a numerical constant which was derived in Paper I.

In the following subsections, we derive this approximate solution. According to the procedure described in Appendix B of Paper I, the profile of the surface current is expanded in a power-law series in r . Then, Biot-Savart Equation (16) is integrated to obtain the disk potential ψ_d . The disk potential should be in a quadratic form of r , which determines the profile of the surface current.

Solutions near the Outer Boundary

Following Paper I, the surface current near the outer boundary r_{out} is expanded as

$$K_\phi(r') = A_{out} r'^{-2} \left[a_0 + \sum_{m=0}^{\infty} a_{2m+1} \left(\frac{r'}{r_{out}} \right)^{2m+1} \right]. \quad (\text{A4})$$

The expansion starts from r^{-2} . For positive D cases described in Paper I, it is expected that $K_\phi \propto r^{-2}$ for $r \ll r_{out}$. However, as shown in Figure 10, the surface current $K_\phi \propto B_z$ is proportional to r if D is negative. We show below that $a_0 = a_1 = 0$ and actually $K_\phi \propto r$ for $r \ll r_{out}$. Integration of Biot-Savart Equation (16) gives the disk potential

$$\begin{aligned} \psi_d = & \frac{2\pi A_{out} a_0}{c} + \frac{2\pi A_{out} a_1 r}{c r_{out}} \\ & + \frac{\pi A_{out}}{c} \sum_{n=0}^{\infty} c_n \left(\frac{r}{r_{out}} \right)^{2(n+1)} \left[-\frac{a_0}{2(n+1)} + \sum_{m=0}^{\infty} \frac{a_{2m+1}}{2(m-n)-1} \right], \end{aligned} \quad (\text{A5})$$

where the Laplace coefficients $c_n = [(1/2)_n (3/2)_n] / [(1)_n (2)_n]$ and $(a)_n = a(a+1) \cdots (a+n-1)$. The disk potential should have a quadratic form of r as

$$\psi_d = \psi_{in} - \frac{1}{2} B_\infty r^2. \quad (\text{A6})$$

Further, as seen in Figure 10, ψ_{in} must be negligible compared to the external flux $\frac{1}{2} B_\infty r^2$. Equating Equation (A5) and Equation (A6) with $\psi_{in} = 0$ gives the conditions on the coefficients a_{2m+3} as

$$a_0 = a_1 = 0, \quad (\text{A7})$$

$$\sum_{m=1}^{\infty} \frac{a_{2m+3}}{2(m-n)-1} = \frac{a_3}{2n+1} \quad \text{for } n \geq 0. \quad (\text{A8})$$

In deriving Equation (A8), the indexes m and n were replaced by $m-1$ and $n-1$, respectively. When Equations (A7) and (A8) are satisfied, the disk potential becomes

$$\psi_d = \frac{\pi A_{out}}{c} \left(\frac{r}{r_{out}} \right)^2 \left[a_3 + \sum_{m=1}^{\infty} \frac{a_{2m+3}}{2m+1} \right]. \quad (\text{A9})$$

Condition for the coefficients a_{2m+3} in Equation (A8) is the same as the condition at the inner boundary for $D > 0$ cases treated in Paper I. Comparing Equation (A8) to Equations (B23) and (B26) in Paper I, we find that

$$\frac{a_{2m+3}}{a_3} = \frac{(-1)^m}{m!} \frac{\Gamma(1/2)}{\Gamma(1/2-m)}, \quad (\text{A10})$$

where we used $\kappa = 1/2$. Inserting this expression to Equation (A9) and using

$$\sum_{m=1}^{\infty} \frac{a_{2m+3}/a_3}{2m+1} = \frac{\pi}{2} - 1, \quad (\text{A11})$$

the disk potential reduces to

$$\psi_d = \frac{\pi^2 A_{out} a_3}{2c} \left(\frac{r}{r_{out}} \right)^2. \quad (\text{A12})$$

Equating Equations (A6) and (A12), we find $2\pi A_{out} a_3/c = 2B_{\infty} r_{out}^2/\pi$. From Equations (A1) and (A4), the vertical field strength for $r_{in} \ll r < r_{out}$ is

$$B_z = \frac{2}{\pi} |D| B_{\infty} \left(\frac{r}{r_{out}} \right) \left[1 - \left(\frac{r}{r_{out}} \right)^2 \right]^{-1/2}, \quad (\text{A13})$$

where we used $[1 - (r'/r_{out})^2]^{-1/2} = 1 + \sum_{m=1}^{\infty} (a_{2m+3}/a_3)(r'/r_{out})^{2m}$ (see Equations (B21) and (B24) in Paper I).

Solutions near the Inner Boundary

Near the inner boundary r_{in} , the surface current is expanded as

$$K_{\phi}(r') = A_{in} r' \left[1 + b_2 \left(\frac{r'}{r_{in}} \right)^{-2} + \sum_{m=1}^{\infty} b_{2m+1} \left(\frac{r'}{r_{in}} \right)^{-(2m+1)} \right], \quad (\text{A14})$$

where we used the fact that $K_{\phi} \propto r$ for $r \gg r_{in}$, and $b_1 = b_4 = b_6 = b_8 = \dots = 0$ for convergence of integration in Equation (16). The disk potential is

$$\begin{aligned} \psi_d = & \frac{\pi A_{in} r_{in}^3}{c} \left\{ 2b_2 \left(\frac{r}{r_{in}} \right) + 2b_3 - \sum_{n=0}^{\infty} c_n \left(\frac{r}{r_{in}} \right)^{-(2n+1)} \right. \\ & \times \left[\frac{1}{2(n+2)} + \frac{b_2}{2(n+3)} + \sum_{m=1}^{\infty} \frac{b_{2m+1}}{2(n-m)+3} \right] \left. \right\} \\ & + \frac{\pi A_{in} r_{out}^3}{c} \left(\frac{r}{r_{out}} \right)^2, \end{aligned} \quad (\text{A15})$$

where we used $r_{out} \gg r$. This expression must be equal to Equation (A6). Note that, as shown in Figure 10, total magnetic flux can be treated as a constant ψ_{in} near the inner boundary $r_{in} \leq r \ll |D|^{-1/3} r_{in}$. We find

$$b_2 = 0, \quad (\text{A16})$$

$$\sum_{m=1}^{\infty} \frac{b_{2m+1}}{2(m-n)-1} = \frac{b_0}{2(n+1)} \quad \text{for } n \geq 1. \quad (\text{A17})$$

When deriving Equation (A17) the index n was replaced by $n-1$. The above conditions are the same as that of the outer boundary cases for $D > 0$ treated in Paper I. Comparing Equation (A17) to Equations (B15) and (B17) in Paper I, we find that

$$b_{2m+1} = \frac{(-1)^m}{m!} \frac{\Gamma(\gamma_c + 1)}{\Gamma(\gamma_c + 1 - m)}, \quad (\text{A18})$$

where $\gamma_c = 0.43$. Equating Equation (A15) and Equation (A6), and using $b_3 = -\gamma_c$, the disk potential becomes

$$\psi_d = \frac{\gamma_c B_{\infty} r_{in}^3}{r_{out}} - \frac{B_{\infty} r^2}{2}. \quad (\text{A19})$$

The total flux is

$$\psi = \gamma_c \left(\frac{r_{in}}{r_{out}} \right) B_{\infty} r_{in}^2. \quad (\text{A20})$$

Equation (A20) shows that the total magnetic flux inside r_{in} is reduced by a factor of $2\gamma_c(r_{in}/r_{out})$ from the flux of the external field. Assuming constant field strength for $r < r_{in}$, B_z is approximately written as

$$B_z \approx 2\gamma_c \left(\frac{r_{in}}{r_{out}} \right) B_{\infty}. \quad (\text{A21})$$

Note that Equation (A21) is a crude estimate because r -dependence of B_z near r_{in} is neglected.

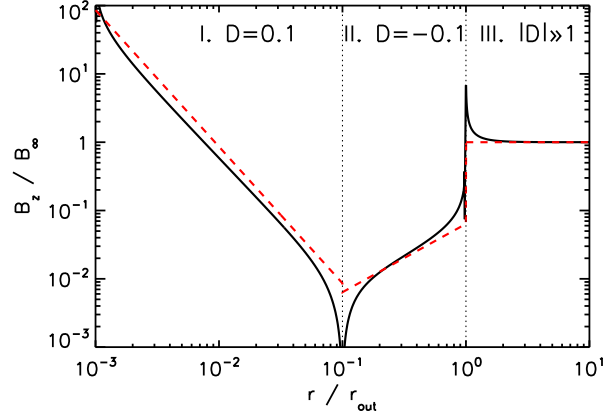


Figure 11. Steady profile of the magnetic field for piecewise constant D . The solid line is numerically calculated, and the dashed line shows the approximate expression given by Equation (A23).

Magnetic Field Profile When Both Inward and Outward Advections Exist

Using the results described above and in Paper I, we can construct approximate expressions for magnetic field profiles in disks where both inward and outward advections exist. We consider the case,

$$D = \begin{cases} D_I > 0 & \text{for } r < r_{disk} \\ D_{II} < 0 & \text{for } r_{disk} < r < r_{out} \\ \infty & \text{for } r > r_{out} \end{cases} \quad (\text{A22})$$

The magnetic field profile can be determined from the outside. For $r > r_{out}$, the magnetic field is constant B_∞ . For $r_{disk} < r < r_{out}$, the profile is given by Equation (A13). For $r < r_{disk}$, the profile is given by Equation (40) of Paper I with a modification that the total flux is reduced by a factor $2\gamma_c(r_{disk}/r_{out})$. Thus, B_z is written as

$$B_z = \begin{cases} 2\gamma_c |D| \left(\frac{r_{disk}}{r_{out}}\right) \left(\frac{r}{r_{disk}}\right)^{-2} B_\infty & \text{for } r < r_{disk} \\ \frac{2|D|}{\pi} \left(\frac{r}{r_{out}}\right) B_\infty & \text{for } r_{disk} < r < r_{out} \\ B_\infty & \text{for } r > r_{out} \end{cases} \quad (\text{A23})$$

This approximate expression is compared to the numerical result in Figure 11. Some differences between the approximate formula and the numerical result are apparent. For $r < r_{disk}$, Equation (A23) gives smaller B_z than the numerical result by a factor $0.64 \approx 2/\pi$, implying that a more rigorous treatment at r_{disk} is required. Approximate Equation (A23) (and (28) in the main text) should be considered to have errors by a factor of ≈ 2 .

REFERENCES

- Bai, X.-N., & Stone, J. M. 2013, *ApJ*, 769, 76
Balbus, S. A., & Hawley, J. F. 1998, *Reviews of Modern Physics*, 70, 1
Bisnovaty-Kogan, G. S., & Lovelace, R. V. E. 2012, *ApJ*, 750, 109
Blandford, R. D., & Payne, D. G. 1982, *MNRAS*, 199, 883
Cao, X. 2011, *ApJ*, 737, 94
Cao, X., & Spruit, H. C. 2013, *ApJ*, 765, 149
Dzyurkevich, N., Turner, N. J., Henning, T., & Kley, W. 2013, *ApJ*, 765, 114
Frank, J., King, A., & Raine, D. 1992, *Accretion Power in Astrophysics* (Cambridge: Cambridge Univ. Press)
Fromang, S., & Stone, J. M. 2009, *A&A*, 507, 19
Gressel, O., Nelson, R. P., & Turner, N. J. 2012, *MNRAS*, 422, 1140
Guan, X., & Gammie, C. F. 2009, *ApJ*, 697, 1901
Guilet, J., & Ogilvie, G. I. 2012, *MNRAS*, 424, 2097
Guilet, J., & Ogilvie, G. I. 2013, *MNRAS*, 430, 822
Guilet, J., & Ogilvie, G. I. 2014, *MNRAS*, 441, 852
Hartmann, L., Calvet, N., Gullbring, E., & D'Alessio, P. 1998, *ApJ*, 495, 385
Hawley, J. F., Gammie, C. F., Balbus, S. 1995, *ApJ*, 440, 742
Kitamura, Y., Momose, M., Yokogawa, S., Kawabe, R., Tamura, M., & Ida, S. 2002, *ApJ*, 581, 357
Krasnopolsky, R., Li, Z.-Y., & Blandford, R. 1999, *ApJ*, 526, 631
Lesur, G., & Longaretti, P.-Y. 2009, *A&A*, 504, 309
Lovelace, R. V. E., Rothstein, D. M., & Bisnovaty-Kogan, G. S. 2009, *ApJ*, 701, 885
Lubow, S. H., Papaloizou, J. C. B., & Pringle, J. E. 1994, *MNRAS*, 267, 235
Lynden-Bell, D., & Pringle, J. E. 1974, *MNRAS*, 168, 603
Ogilvie, G. I., & Livio, M. 2001, *ApJ*, 553, 158
Okuzumi, S., & Hirose, S. 2011, *ApJ*, 742, 65
Okuzumi, S., Takeuchi, T., & Muto, T. 2013, *ApJ*, 785, 127
Rothstein, D. M., & Lovelace, R. V. E. 2008, *ApJ*, 677, 1221
Sano, T., Miyama, S. M., Umebayashi, T., & Nakano, T. 2000, *ApJ*, 543, 486
Shibata, K. & Uchida, Y. 1985, *PASJ*, 37, 31
Shu, F. H., Galli, D., Lizano, S., Glassgold, A. E., & Diamond, P. H. 2007, *ApJ*, 665, 535
Simon, J. B., Bai, X.-N., Armitage, P. J., Stone, J. M., & Beckwith, K. 2013, *ApJ*, 775, 73
Suzuki, T. K., Muto, T., & Inutsuka, S.-I. 2010, *ApJ*, 718, 1289
Walsh, C., Nomura, H., Millar, T. J., & Aikawa, Y. 2012, *ApJ*, 747, 114